A corrosion cracking mechanism-based model with molten salt corrosion damage coupling the effect of chloride impurity and plastic deformation

Heng Li [a b], Yan He [a b], Xinyu Yang [c], Dewen Zhou [a b], Xiaowei Wang [a b], Jianqun Tang [a b], Jianming Gong [a b]

[a]

School of Mechanical and Power Engineering, Nanjing Tech University, Nanjing, 211816, China

[b]

Institute of Reliability Centered Manufacturing (IRcM), Nanjing Tech University, Nanjing, 211816, China

[c]

Institute of High Performance Computing (IHPC), Agency for Science, Technology and Research (A*STAR), 1 Fusionopolis Way, #16-16 Connexis, 138632, Republic of Singapore

Abstract

The corrosion kinetic models, incorporating the effects of chloride impurity and plastic deformation were proposed. Molten salt corrosion (MSC) damage was quantitatively described using the corrosion kinetic and the distance of materials points from the corrosion surface. By employing the elastic-viscoplastic theory with a hyperbolic-sine flow rule and the proposed damage model, a corrosion cracking mechanism-based model was developed and implemented using finite element (FE) analysis method. The corrosion-assisted cracking ahead of crack tips in accordance with the corrosion cracking mechanism was simulated. Furthermore, the predicted corrosion depth, corrosion morphologies, and multi-site corrosion cracking behaviors showed good agreement with the experimental results.

Keywords

Damage model

Corrosion cracking

Corrosion kinetic model

SSRT

Molten salt corrosion

Nomenclature

ε

Total strain tensor

εe

Elastic strain tensor

εp

Plastic strain tensor

E

Elastic modulus

σ

Stress tensor

$\tilde{\sigma}$

Effective stress

$\tilde{\sigma}'$

Effective stress deviator

DTOT
Total damage
I
Identity tensor
fy
Yield function
RH
Isotropic hardening stress
σy0
Initial yield stress
Q
Saturated isotropic hardening stress
B
The rate sensitivity exponential for RH to reach Q
n
Normal direction
p
Accumulated plastic strain rate
θ
Temperature dependent material parameters
ϕ
Temperature dependent material parameters
htot
Total oxide thickness
t
Time
kp0
Corrosion rate constant
kpCl
Corrosin rate constant caused by chloride impurity
JFeCl2
Diffusion flux of metal chloride
Sp
Stress-diffusion coupling factor
DMECH
Mechanical damage
xi
Distance of element from the surface
DTOT
Total damage
CFeCl2
Concentration of $FeCl_2$ in C/S interface
DFeCl2
Diffusion coefficient of $FeCl_2$ in the oxide layer

n

Moles of metal chlorides

Vm

Molar volume of metal chlorides

λ

Material constant

Jx, Jd, Jm

Flux in x direction, diffusion flux and migration flux, respectively

Be, Bm

Absolute ionic mobility and absolute electrical mobility, respectively

De

Diffusion coefficient of ions

μ

Chemical potential

ψ

Particle conductivity

Dc

Diffusion coefficient of cations

R

Gas constant

Δμ

Chemical potential difference

$\bar{\mu}$

Stress-affected chemical potential

σm

Absolute value of the spherical stress

Δεp

Increment of plastic strain

$\bar{\bar{\mu}}$

Deformation-affected chemical potential

kpGR

Corrosion rate parameter of grian under plastic deformation

kpGB

Corrosion rate parameter of GB under plastic deformation

DMSC

MSC damage

rn

A set of random numbers

DTH

Damage threshold

DTHrnd

Random damage threshold

hGR

Thickness of corrosion layer for grain

hGB
Thickness of corrosion layer for GB
c
Thickness of the corrosion-affected layer
Rv
Stress triaxial factor

1. Introduction

In the context of striving for carbon neutrality, there is a discernible shift towards the gradual replacement of conventional energy sources with renewable energy for power generation. However, renewable energy sources such as wind, solar power, and tidal energy, are characterized to as intermittent due to there irregular availability and predictability [1]. To address the intermittency challenge and bridge the gap between electricity supply and demand, molten-salt-based thermal energy storage (TES) emerges as a pivotal solution in the integration of renewable energy. TES is primarily integrated into concentrated solar power (CSP) plants for thermal energy storage during the day and releasing heat during the night, distinguishing CSP from other renewable energy options [2]. The flexibility of nuclear power generation may also be increased by integrating TES with nuclear reactor technology [3]. A standalone TES system for electricity storage can be attractive due to a continuing cost drop of wind and solar power, and the need for dispachable renewable generation [4]. The growing role of TES among energy storage technologies has increased the importance of understanding its long-life design, which requires further understanding of the failure modes of components in TES.

The primary concerns regarding the failure or deterioration of components within TES revolve around two key factors: the high-temperature corrosion caused by molten salt and stress/deformation from mechanical load, self-weight, residual stress, etc. These two factors can independently degrade the structural material, resulting in surface corrosion depletion or the accumulation of plastic damage. However, the premature failure of structural materials could be caused by the coupling effect of molten salt corrosion (MSC) and stress/deformation. The failure mechanism of materials subjected to coupling effects differs from that of MSC or accumulated plastic damage. Corrosion cracking is a typical characteristic of structural material, especially for austenitic stainless steel which has been widely used in TES systems. Hence, it is critically important to investigate the coupling effect of MSC and stress/deformation and to reveal the corrosion cracking mechanism of the structural steel.

Many researchers have explored the corrosion behavior of austenitic stainless steels in molten salt, particularly focusing on solar salt, the most popular salt used in commercial TES. Considering the primary chloride impurity introduced by the manufacturing process, several studies have examined the corrosion behavior and mechanisms of structural materials such as low alloy steel, austenitic stainless steel, and nickel-based alloys in solar salt with varying chloride content. The active corrosion mechanism [5] is the most accepted theory to explain the accelerated effect of chloride on corrosion. However, few studies focus on the interaction effect of MSC and mechanical load on the mechanical properties of structural materials in TES. Slow strain rate tensile (SSRT) testing is a popular method for studying stress corrosion cracking, which reflects the coupling effect of corrosion environment and mechanical load on material properties. Goods [6] carried out a series of SSRT tests for alloy 800 in molten solar salt at 600 °C. The results demonstrated no appreciable loss of ductility compared to that in air. However, SSRT tests on 2.25Cr-1Mo in molten salt at 525 °C revealed that pronounced ductility loss and the formation of a non-adherent, easy-spalled oxide

layer [7]. These studies did not consider the effects of chloride impurity on the mechanical behaviors of the materials. Pineda et al. [8] performed the electrochemical impedance spectroscopy (EIS) and SSRT tests for VM12 martensitic steel in lithium nitrates indicating that MSC reduced strength and elongation. Mallco et al. [9] concluded that the mechanical properties of T91 steel degrade in lithium nitrates at 550 °C. However, these studies provided little microstructural information on the failure mechanisms. Li et al. [10] carried out SSRT tests for 304 and 316L stainless steels in molten solar salt containing different contents of chloride impurity. The corrosion-mechanical behaviors of the steels were studied and a model was proposed for predicting deformation considering MSC. The results also revealed that MSC behavior was significantly affected by the SSRT. Nevertheless, there is scarce literature modeling the corrosion crack growth behavior and, the interaction between tensile load and MSC. In addition, few studies have developed an MSC kinetic model to capture the effect of chloride impurity, which is crucial for predicting the corrosion rate and corrosion cracking behavior of structural materials subjected to MSC and mechanical load.

Owing to the difficulties in testing the initiation and growth of corrosion cracks under the interaction of the harsh molten salt environment and tensile load, conclusive results have been limited. Using finite element models to examine fracture mechanics problems across a range of length scales and mechanisms, it is possible to model the damage development due to the combined effects of MSC and tensile deformation. Biglari et al. [11] investigated the crack growth due to oxidation-creep interaction using the linear accumulation of damage,describing oxidation damage evolution by the parabolic law. Efforts to explore the crack growth caused by oxidation-carburization-creep [12], and oxidation-creep-fatigue interaction [13] using various models exist. These studies adopt an environmental damage modelthat follows the parabolic law. In reality, stress and plastic deformation can affect the oxidation/corrosion behavior of structural materials by accelerating corrosion depletion and/or leading to different corrosion morphologies. However, few studies have reported the MSC kinetic models considering stress/deformation and chloride impurity. In addition, MSC-assisted cracking ahead of crack tips was not considered in the above investigations.

In the present work, the corrosion kinetic models were proposed for both grain and grain boundary (GB) with consideration of stress, deformation, and chloride impurity. Meanwhile, a damage model for MSC was developed. All models were implemented in user subroutines UMAT and USDFLD. The modeling is presented to predict the MSC and cracking behaviors of austenitic stainless steel in molten solar salt. The proposed model was verified by the experimental results, continuing of our previous work.

2. Experiments

2.1. Materials and methods

The experimental procedures are illustrated in Fig. 1. $NaNO_3$, KNO_3 and NaCl were separately kept in a muffle furnace at 150 °C for 2 h to remove moisture. Then, 0, 0.6, 1.0 and 1.4 wt% of high-grade NaCl were deliberately added to the binary nitrate salt (60 wt% $NaNO_3$ + 40 wt% KNO_3) to form salt mixtures SS, SS_0.6, SS_1.0 (the maximum impurity contents in commercial nitrate salts [14,15]) and SS_1.4, simulating the solar salt with different contents of chloride impurity.

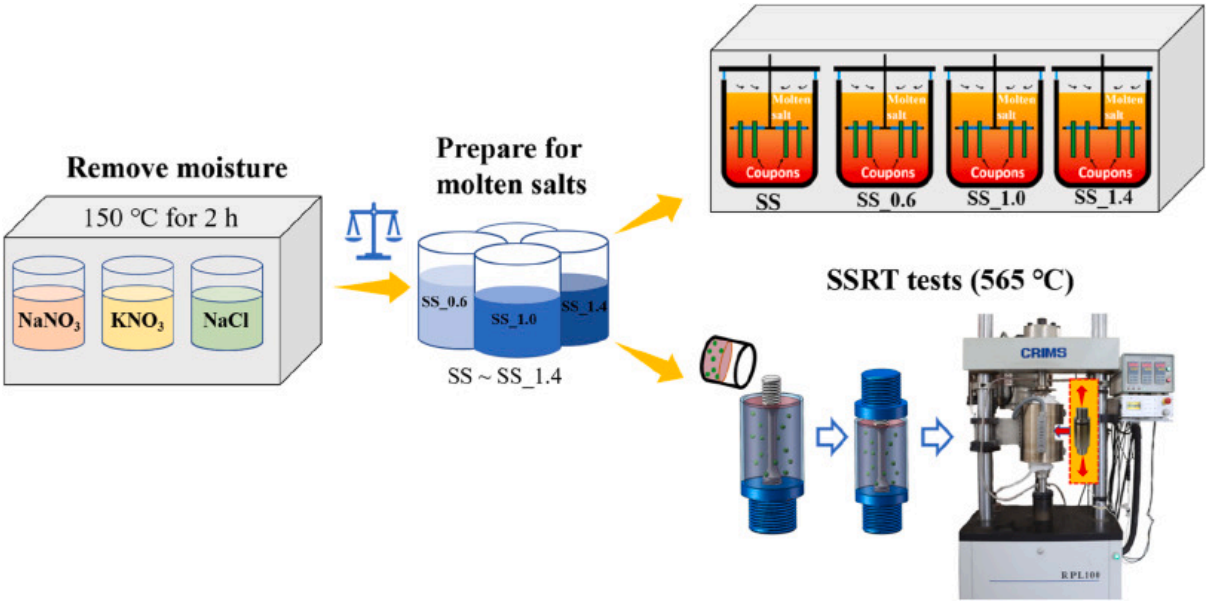

1. Download: Download high-res image (623KB)
2. Download: Download full-size image

Fig. 1. Schematic diagram of long-term corrosion tests and SSRT tests.

Isothermal long-term corrosion tests were carried out on 304 stainless steel in binary nitrate salts containing different impurity contents. Rectangular samples measuring 20 mm × 10 mm × 3 mm were cut from sheets using electric discharge machine. Samples were immersed in alumina crucibles containing the prepared molten salt mixtures. Isothermal long-term corrosion tests were carried out Two samples were extracted at time intervals of 500, 1000, 1500, 2000 and 3000 h to measure the weight loss and perform characterization. More details about the long-term corrosion test can be found in Refs. [16,17].

Slow strain rate tensile (SSRT) tests were carried out for 304 steel in salt mixtures SS, SS_0.6, SS_1.0 with a specially designed fixture at 565 °C. A tensile load with the strain rate of 5.56×10^{-7}/s was applied to the sample. Besides, interrupted tests were performed for 304 steel at 30 %, 75 % and 90 % of rupture strain in solar salt containing 1.4 wt% NaCl to investigate microcrack initiation and propagation. Molten salts were poured out into the container of specially designed fixture, which had been integrated with the test sample. After cooling down, the other side of the sample was fixed by an upper clamp and the standards SSRT tests were performed on SINATEST EQUIPMENT RPL100. The detailed testing methods for SSRT can be found in our previous works [10,16].

Before microstructural characterization, the remaining salts were removed from the surface of the tested samples by rinsing them with warm distilled water. A thin nickel plate was coated on the cleaned sample to protect the corrosion layer from descaling during metallographic preparation. The cross-sectional morphologies were observed by field emission scanning electron microscope (FE-SEM) using Zeiss Ultra 55 equipped with energy dispersive spectroscopy (EDS). To obtain the quantitative distribution of alloy elements in the corrosion layer, a JEOL iHP200F Electron Probe Micro Analyzer (EPMA) was used to characterize the corrosion layer at 15kV acceleration voltage. Due to the completion of the previous mechanical tests, the experiments in present work mainly focus on microstructural characterization to provide a data foundation for subsequent model predictions.

2.2. Experimental results

2.2.1. Long-term corrosion test

Fig. 2 shows the corrosion kinetics curves [16] of 304 steel in different salts. It is clear that chloride impurity leads to higher metal loss after the same duration. Even when the concentration of chloride impurity reaches 1.4 wt%, the corrosion behavior of 304 exhibits parabolic kinetics with a solid-state diffusion mechanism. The corresponding parabolic corrosion rate constant kp0 of 304 in different salts, is also presented in Fig. 2 (the bar chart). It shows a significant dependence of corrosion kinetics on chloride concentration. The higher corrosion rate caused by chloride impurity is attributed to the "active corrosion" mechanism [[17], [18], [19]], which asserts that the formation and oxidation of metal chlorides accelerate the growth of corrosion layer. Fig. 3 shows the element distribution map and the quantitative line scan for 304 steel after 3000 h of immersion in molten SS_1.4 salt at 565 °C. A typical multi-layer corrosion product formed on the studied steel. The outer layer primarily consists of iron oxide, whereas the inner layer consists of iron-chromium oxide. Underneath the corrosion layer, there is a "nickel rich/chromium depletion area" approximately 4 μm in width, resulting from the dissolution of chromium in the melt [20].

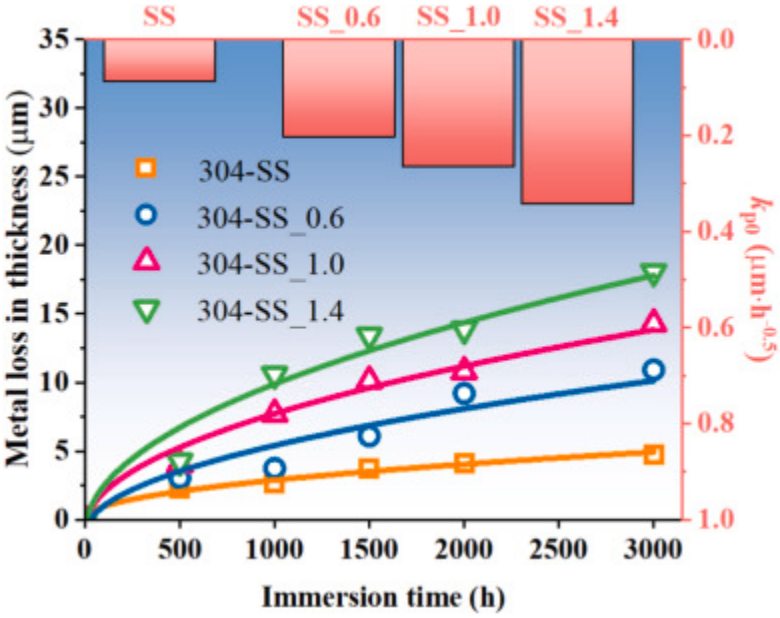

1. Download: Download high-res image (405KB)
2. Download: Download full-size image

Fig. 2. Corrosion kinetic curves of 304 steel in different salts [16].

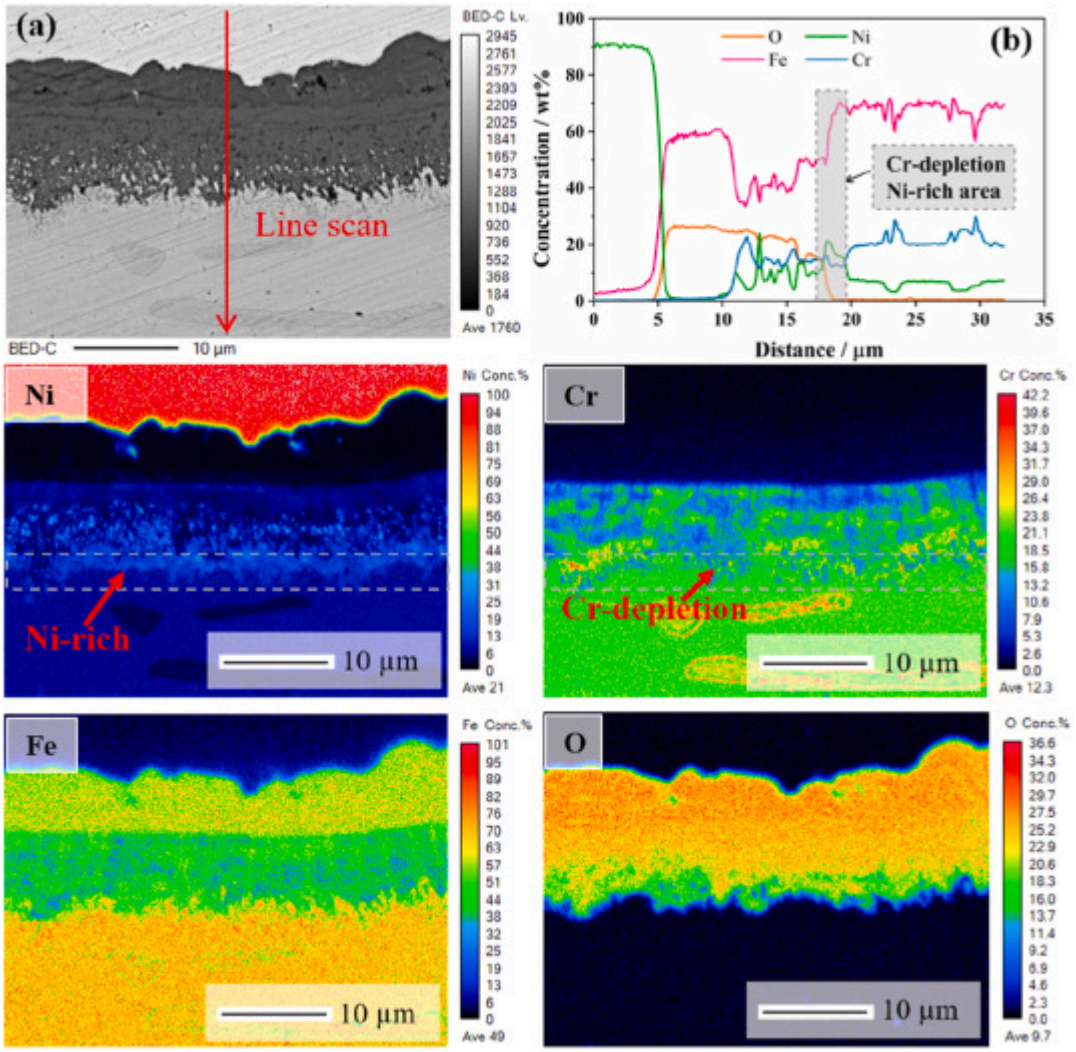

1. Download: Download high-res image (2MB)
2. Download: Download full-size image

Fig. 3. Typical multi-layered corrosion layer on 304 steel immersed in SS_1.4 for 3000 h.

2.2.2. SSRT test

Fig. 4 shows the interrupted tested curves and tensile curves of 304 steel in different environments [10]. The yield strength and ultimate tensile strength are negligibly affected by MSC whereas the uniform elongation significantly decreases with the increasing concentrations of chloride. The corrosion products crack at grain boundaries (GBs), promoting the initiation and propagation of microcracks at GBs [10]. Chloride impurity accelerates corrosion of GBs, leading to higher ductility loss. Fig. 5 illustrates the corrosion kinetic curves of 304 steel obtained from SSRT test and corrosion test. The comparison indicates that plastic deformation can significantly accelerate the corrosion of 304 steel. The degradation of the mechanical properties is attributed to the coupling effects of plastic deformation and MSC, as well as the presence of chloride impurity.

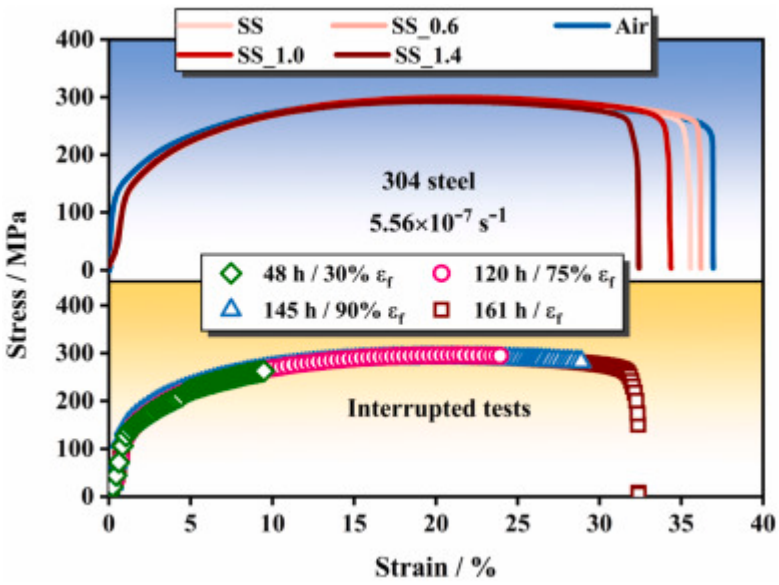

1. Download: Download high-res image (372KB)
2. Download: Download full-size image

Fig. 4. Tensile curves of 304 steel in different environments [10].

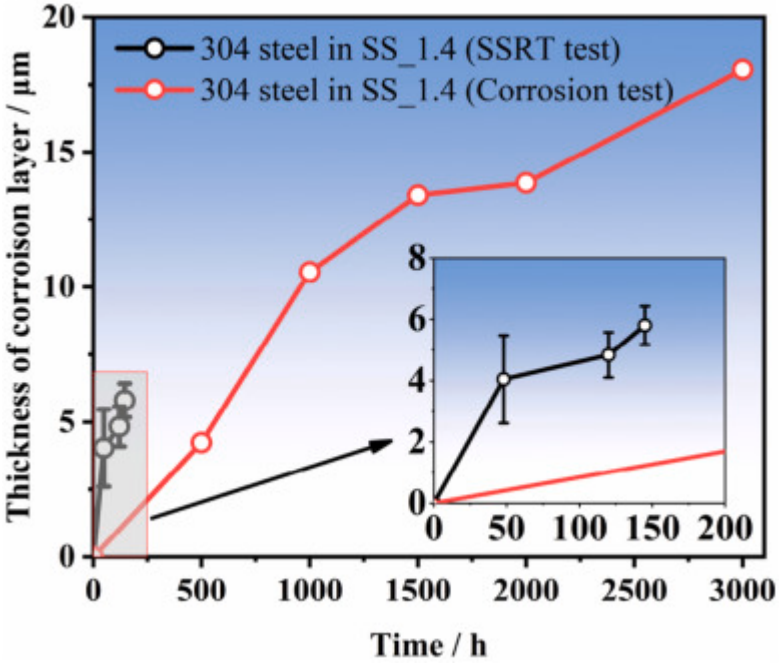

1. Download: Download high-res image (378KB)
2. Download: Download full-size image

Fig. 5. Comparison of corrosion kinetic curves of 304 steel between long-term corrosion test and SSRT test at 565 °C.

Fig. 6 shows the cross-sectional morphologies of the corresponding tested sample from interrupted SSRT tests. The evolution of corrosion and cracking at GBs can be clearly observed. At the initial stage of SSRT in molten salt, few microcracks are found, butcorrosion products form on the surface. Corrosion at GBs occurs due to the accumulation microstructural features such as dislocations and dislocation substructures in the GB under plastic deformation, which act as the short diffusion tunnel for the chemical ions [21]. Under continuous deformation, the fragile corroded GB will crack, exposing fresh substrate ahead of the crack tip. The penetration of molten salt will lead to further

corrosion at the crack tip. This process repeats, ultimately causing extensive corrosion and cracking of the GBs.

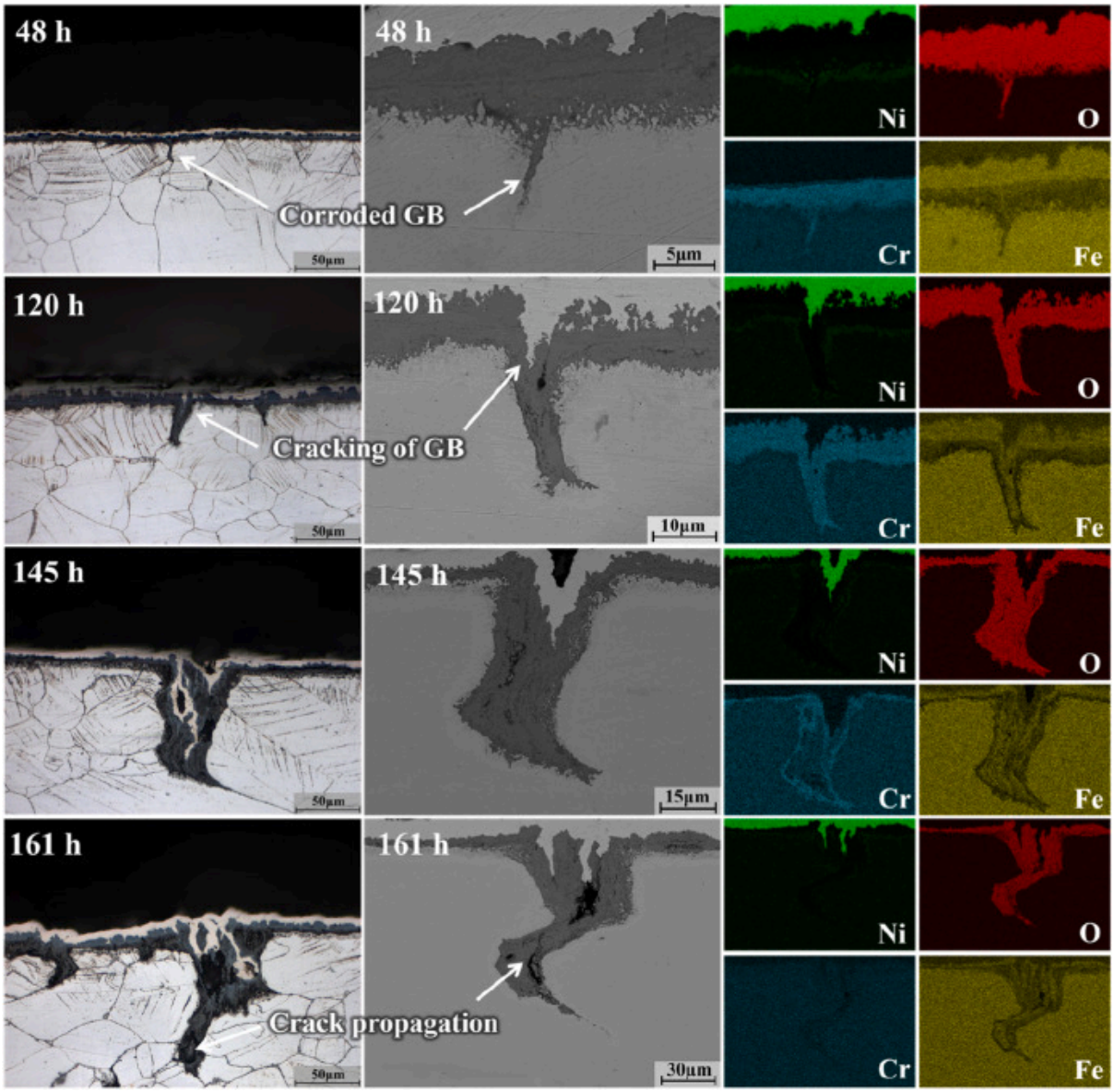

1. Download: Download high-res image (2MB)
2. Download: Download full-size image

Fig. 6. Evolution of corrosion cracks along GBs at 48 h [10], 120 h, 145 h [10] and 161 h, respectively.

3. Material model

The prediction of corrosion cracking of the studied steel in high-temperature molten salt environment is essentially a problem involving the interaction between electrochemical process and mechanical behaviors. Electrochemical corrosion behavior can affect mechanical behavior by reducing the bearing area of materials, promoting crack propagation, and changing the fracture mode. In this work, the degradation of the studied steel in molten salt can be attributed to these effects. On the other hand, mechanical behavior can also affect the corrosion rate and behavior of the material. However, few numerical models consider the effect of mechanical behavior on the corrosion kinetic of materials in molten salt. In this section, a mechanical model is first presented to simulate the deformation behavior. Then, MSC kinetic models are proposed, coupling the effects of chloride

impurity and plastic deformation. An MSC damage model is further proposed based on the corrosion kinetic model. By incorporating a plastic damage model, corrosion cracking modeling can be performed using finite element analysis.

3.1. Constitutive equation

Within the framework of visco-plasticity, the total strain is assumed to be decomposed into an elastic strain and plastic strain:(1)ε=εe+εp

According to Hooke's law, the elastic strain is given as:(2)εe=1+vEσ˜−vETr(σ˜)Iwhere σ˜=σ/(1−DTOT), is the effective stress. DTOT represents the total damage including mechanical damage and MSC damage. I is the identity tensor. The yield function is described by introducing the concepts of isotropic hardening RH and initial yield stress σy0:(3)fy=J2(σ'˜)−RH−σy0where σ'˜ and J2(σ'˜) represent the effective stress deviator and effective equivalent stress, respectively. The expressions of σ'˜, J2(σ'˜) and RH are as follows:(4)σ'˜=σ˜−13Tr(σ˜)I(5)J2(σ'˜)=32(σ'˜:σ'˜)(6)RH=Q(1−e−Bp)where *Q* is the saturated value of isotropic hardening, *B* is the rate sensitivity exponential for RH to reach *Q*. Due to the normality rule, the rate of plastic deformation is the product of the normal direction n=σ'˜J2(σ'˜) and the accumulated plastic strain rate p˙:(7)ε˙p=p˙n

The value of the accumulated plastic strain rate p˙ is given by the hyperbolic sine function, which has the benefit of high accuracy for a wide range of strain rates [22]:(8)p˙=θsinh(ϕfy)where θ and ϕ are temperature dependent material parameters.

3.2. The proposed corrosion kinetic model

3.2.1. The effect of impurity on corrosion kinetic

In pure molten solar salt, the growth of the corrosion layer on austenitic stainless steel is controlled by ions diffusion, showing the parabolic corrosion kinetics. According to the solid-state diffusion mechanism [23], the total oxide thickness htot is given as:(9)dhtotdt=kp0htotwhere kp0 represents the corrosion rate constant and, *t* is time. With the presence of chloride impurity in molten nitrate salt, the corrosion of austenitic stainless steel is driven by both the solid diffusion mechanism and the active corrosion mechanism, as illustrated in Fig. 7 (taking the reactions of the iron element as an example, which is also the main element in the studied steel). The active corrosion mechanism includes four steps [5]: S1, formation of Cl_2; S2, penetration of Cl_2 into oxide/substrate; S3, reaction of Cl_2 with metal atom; S4, formation of metal chlorides, which are then oxidized to form oxide and Cl_2. Hence, the oxide thickness htot' becomes:(10)dhtot'dt=(dh'totdt)0+(dh'totdt)Cl=kp0htot'+kpClhtot'where kpCl is the corrosion rate constant caused by chloride impurity. The outward diffusion and oxidation of metal chlorides lead to the rapid growth of the oxide layer. This process is primarily controlled by the diffusion of metal chloride, as the rate of charge transfer is much higher than the diffusion rate of metal chloride. The diffusion flux of metal chloride JFeCl2 is:(11)JFeCl2=DFeCl2CFeCl2htot'where CFeCl2 represents the concentration of $FeCl_2$ in C/S interface. DFeCl2 is the diffusion coefficient of $FeCl_2$ in the oxide layer. Accordingly, the growth rate of oxide layer caused by chloride impurity can be defined by:(12)(dh'totdt)Cl−=nVmJFeCl2=nVmDFeCl2CFeCl2htot'where *n* and V_m are the moles and molar volume of metal chlorides, respectively, which can be assumed as constants when the chloride concentration is determined and the temperature remains constant, as well as DFeCl2. Then, Eq. (12) becomes:(13)(dh'totdt)Cl−=λ0CFeCl2htot'where, λ0=nVmDFeCl2 is assumed to be a constant.

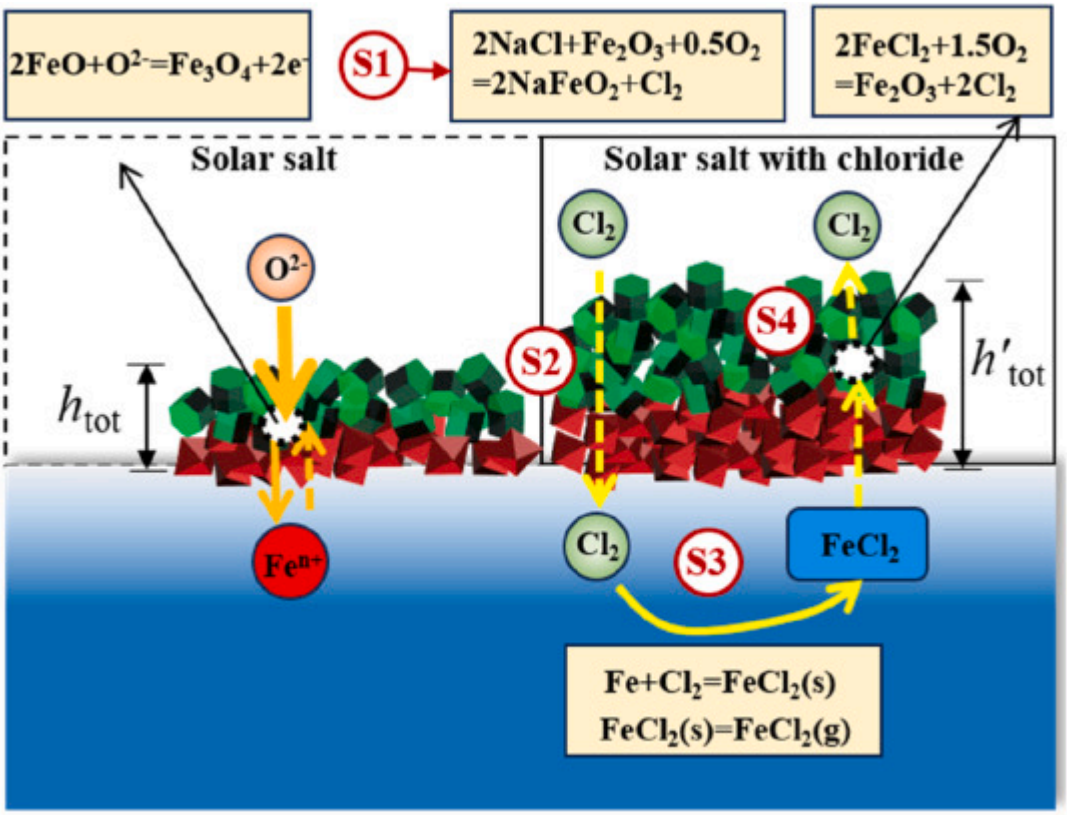

1. Download: Download high-res image (592KB)
2. Download: Download full-size image

Fig. 7. Corrosion mechanism of stainless steel in molten solar salt containing chloride impurity (take the reactions of the iron element as an example, which is also the main element in the studied steel).

According to the chemical reactions in step 3 (S3 in Fig. 7), the concentration of $FeCl_2$ depends on the concentration of Cl_2 (CCl2), while the concentration of Cl_2 is related to the activity of Cl^- (aCl−)in molten salts. Then, Eq. (13) becomes:(14)(dh'totdt)Cl−=λ0CFeCl2htot'=λ0'CCl2htot'=λ0'aCl−/htot'=λ0'faCCl−/htot'where λ0' is a constant; fa is the activity coefficient of Cl^-, which is assumed as a constant when the corrosive medium remains stable. Then, Eq. (14) becomes:(15)(dh'totdt)Cl−=λCCl−htot'where λ=λ0'fa is a parameter that depends on the material and environmental conditions. Substituting Eq. (15) into Eq. (10) yields:(16)dhtotdt=kp0+λCCl−htot=kptothtotHence, when the molten salt contains the chloride impurity, the corrosion rate parameter kptot can be determined by the intrinsic MSC rate constant kp0 and the impurity concentration:(17)kptot=kp0+λCCl−

3.2.2. The effect of deformation on corrosion kinetic

Corrosion of austenitic stainless steel in molten salt is primarily an electrochemical process involving ionic diffusion and migration. The force gradient acting on a moving species consists of migration and diffusion. Hence, the total flux in the x-direction Jx is [24].(18)Jx=Jd+Jm(19)Jd=−CBeNAdμdx(diffusion)(20)Jm=−(zqe)CBmdΦdx(migration)where, Jd and Jm are the diffusion and migration flux. C is the atomic concentration. Be and Bm are the absolute ionic mobility and absolute electrical mobility, respectively. De is the diffusion coefficient of ions. zqe is the particle charge. dμdx and dΦdx are the negative chemical potential gradient and negative electric potential gradient in the x-direction, respectively. Combining

Eqs. (18), (19), (20) yields the total flux due to potential gradient:(21)Jx=−ψ(zqe)2[dμdx+(zqe)dΦdx]where ψ=(zqe)2CDe/(kT) is the particle conductivity. The corrosion product on iron-based steel in molten salt is primarily iron-oxide. To simplify the analysis, the corrosion layer is assumed to consist of a single-phase oxide (iron oxide, for example). Thus, the ionic flux balance for outward cations (zcJc), inward anions (zaJa) and electrons (zeJe) along with ze=1 are [25]:(22)zcJc=zaJa+zeJeFor ionic electroneutrality, Eq. (22) can be further simplified by letting Ja=0. Combining Eqs. (21), (22) yield the negative electric potential gradient dΦdx:(23)dΦdx=ψeqe(ψc+ψe)[dμedx−ψczcψedμcdx]

Inserting Eq. (23) into Eq. (21) and replacing Jx by Jx,c yield the cation vacancy flux in terms of electric conductivity:(24)Jx,c=−ψcψe(zcqe)2(ψc+ψe)dμdxFor a simple oxidation reaction, ψe≫ψc and ψe≈1. Eq. (24) becomes:(25)Jx,c=−1xψc(zcqe)2∫μiμodμwhere, μi and μo are the chemical potential at the metal/oxide interface and the oxide/medium interface, respectively. Moreover, Jx,c is related to the growth rate of oxide layer:(26)Jx,c=Ccdxdtwhere, Cc is the concentration of cations. Combining Eqs. (25), (26) and inserting ψ=(zqe)2CDe/(kT) yields the growth rate of the oxide layer:(27)dxdt=kpx(28)dxdt=−1x(DckT∫μiμodμ)where kp=−DckT∫μiμodμ is the corrosion rate constant. Dc is the diffusion coefficient of cations.

Therefore, the growth rate of the oxide layer depends on the difference in chemical potentials (μ) of reactants and products. Under stress-free conditions, the chemical potential of metal in a corrosive medium is given as:(29)μ=μ0+RTlnacwhere, μ0 and μ represent the reference chemical potential and chemical potential under stress-free conditions, respectively. R is the gas constant and ac represents the thermodynamic activity of the metal.

Due to the relatively low compressibility of solid metal, the chemical potential difference △μ has a linear relationship with the pressure [26]:(30)Δμ=∫P1P2V0e(−χP)dP≈V0ΔPwhere V is volume, P1 and P2 are pressures at initial and end stages, respectively, and ΔP is the pressure difference, V0 is initial volume, and χ≈10−6 is the compressibility coefficient of solids.

Hence, the stress-affected chemical potential $\bar{\mu}$ is given as [26]:(31)$\bar{\mu}$=μ+Vmσmwhere Vm and σm represent the molar volume of the metal atom and absolute value of the spherical stress, respectively. Under plastic deformation, a chemical potential of dislocation model has been proposed by Gutman et al. [27]:(32)Δμ=RTlnNN0where N0 and N represent the dislocation density under the elastic limit and dislocation density under plastic deformation, respectively. N has the following relationship with N0 [27]:(33)N=N0exp(ndΔτ$\bar{\alpha}$kNmaxT)where nd is the number of dislocations in a dislocation pile-up, Δτ is the hardening stress, $\bar{\alpha}$≈109∼1011cm−2, Nmax is the maximum dislocation density. Accordingly, the macro plastic increment Δεp can be defined as:(34)Δεp=N0$\bar{\alpha}$υ(expndΔτ$\bar{\alpha}$kNmaxT−1)where υ is an orientation-dependent factor. Combining Eq. (31) to (34) yields the deformation-affected chemical potential ═μ═:(35)═μ═=μ+Vmσm+RTln(Δεpε0+1)where ε0 is the corresponding strain at the elastic limit. Further integrating Eq. (35) yields:(36)═══∫μi═μo═dμ═=∫uiμodμ+Vm∫σmiσmodσm+RT∫ΔεpiΔεpoε0Δεp+ε0dΔεpwhere subscript "*o*" and "*i*" represent the corrosion layer/corrosive medium interface and corrosion layer/substrate interface.

Assuming that the corrosion product is brittle and, the corrosion layer can not bear load, then σmo≈Δεpo≈0. Rearranging Eq. (36) yields:(37)═══∫μi═μo═dμ═=∫uiμodμ−Vmσm−RTln(Δεpε0+1)

Replacing ═══∫μi═μo═dμ═ with ∫μiμodμ in Eq. (28) yields the proposed corrosion kinetic model considering the effects of plastic deformation and impurity:(38)dxdt=kpGRx(39)kpGR=−DckT[∫μiμodμ−Vmσm−RTln(Δεpε0+1)]
i.e.:(40)kpGR=kp+DckT[Vmσm−RTln(Δεpε0+1)]where kpGR represents the corrosion rate parameter under plastic deformation. kp is the corrosion rate parameter of grain depending on the impurity concentration, which can be determined by the proposed Eq. (17).
Moreover, GB corrosion of Fe-based steels occurs under continuous deformation in high-temperature corrosive medium. The GB exhibits a higher corrosion rate during deformation, which could result from the stress-assisted grain boundary oxidation (SAGBO) effect. Evans et al. [28] have proposed a stress-diffusion coupling factor Sp to mathematically describe the SAGBO effect, as follows:(41)Sp=x˙σx˙0=exp[σmΩm(Φ−1)kT]where x˙σ and x˙0 represent the oxide growth rate under stress and stress-free conditions, respectively. Φ is the Pilling-Bedworth ratio and, Ωm represents the atom volume. Therefore, the corrosion rate parameter of GB under deformation can be obtained by multiplying kpGR and
factor Sp:(42)kpGB=kpGR·Sp={kp+DckT[Vmσm−RTln(Δεpε0+1)]}exp[σmΩm(Φ−1)kT]
Eq. (42) is the proposed corrosion kinetic model for GB in a high temperature corrosive medium considering the deformation, impurity, and the SAGBO effect.

3.3. Damage evolution

Components in TES system that contact molten salt can be exposed to different damage mechanisms, such as rate-dependent plastic deformation and time-dependent MSC, which can significantly reduce their lifetime inducing premature failure. Mechanical damage, DMECH, caused by thermal load or mechanical load may be simply described as a function of the applied load, σ, and time, t:(43)DMECH=f(σ,t)
For MSC damage, DMSC, is dependent on the distance from the surface, xi, and time, t:(44)DMSC=f(xi,t)
Although mechanical and MSC damage are separate mechanisms, they can interact and affect each other. The development of MSC damage is independent of the applied load, but the resulting surface corrosion layer and corroded GB can be brittle and prone to microcracking, thereby accelerating stress corrosion crack growth by offering preferential crack initiation sites. A linear accumulation of mechanical and MSC damage is used:(45)DTOT=DMECH+DMSC
This linear expression allows the two damaging mechanisms to be combined or to be dealt easily with in cases where one of the two is not acting. More details on the evolution of the two damages are provided in the next sections. The total damage variable DTOT is accumulated for every element at each time increment. Once the local corresponding damage initiation criteria are satisfied, material stiffness is degraded according to:(46)σ=(DTHrnd−DTOT)σ˜where DTHrnd is the random threshold for damage of each element, used to simulate the invariably random attack on material points due to micro-scale level variability. The value of DTHrnd can be determined by introducing a set of random numbers rn:(47)DTHrnd=DTH±rn(48)rn∈(0,10%DTH)where DTH represents the damage threshold which can be determined by tensile test.

3.3.1. MSC damage model

In this section, two different damage evolution laws for grain and GB were proposed, which depend on their different corrosion kinetics as stated in section 3.2. For the solid-state diffusion mechanism, corrosion kinetics can be described by the parabolic corrosion model:(49)hGR=kpGRt(50)hGB=kpGBtwhere hGR and hGB represent the thickness of corrosion

layers for grain and GB, respectively.

It is known that there is no distinct boundary between fully corroded material with uncorroded substrate, but a corrosion-affected interface. Damage of material points in this interface lies in the range of damage threshold DTHrnd to 0, i.e. from corroded surface to substrate. Therefore, in this work, the corrosion damage of grain is defined as follows:(51)DmscGR={DTHrndxi≤hGR(corrosionlayer)DTHrnd(1−x−hGRc)βhGR<xi≤hGR+c(corrosion affectedlayer)0xi>hGR(substrate)where DTHrnd is the random damage threshold of materials point, which will be discussed later. *c* is the width of corrosion-affected layer. β represents the exponent of damage distribution.

As for the GB, the corrosion damage reaches DTHrnd near the corroded surface, while it exhibits a gradient distribution characterization when the distance is higher than the corroded depth.

Accordingly, the corrosion damage evolution of GB is defined as follows:(52)DmscGB={DTHrnd(1−xhGB)βx≤hGB(fullcorroded)DTHrnd(hGBx)βx>hGB(notfullcorroded)

3.3.2. Multiaxial plastic damage model

Using the concept of continum damage mechanics (CDM), the plastic deformation process includes microcrack initiation and propagation, which is essentially a process of energy dissipation. Assuming that the plastic deformation and microplastic deformation primarily lead to the material's inner energy dissipation, the dissipation potential can be defined as follows [29,30]:(53)ϕ=ϕp+ϕD+ϕαwhere ϕp is the von Mises yield function based on plastic coupling damage and corresponding to part of plastic dissipation, ϕD is the damage dissipated potential, ϕα is the micro-plastic dissipated potential.

Furthermore, the law of damage dynamics is provided according to Lemaitre's theory:(54)D˙MECH=−∂ϕ∂Ywhere *Y* represents the release rate of strain energy, defined as:(55)Y=−σeq22E(1−DMECH)2Rvwhere Rv is the stress triaxial factor:(56)Rv=[23(1+v)+3(1−2v)(σmσe)2]

A suitable dissipation potential model that satisfies the assumption of isotropic damage is given by Ref. [31]:(57)ϕ=Y22S0p˙(1−DMECH)α0

Combining Eq. (54) to (57) and yields the damage rate D˙MECH:(58)D˙MECH=σeq2Rv2ES0(1−DMECH)2p˙(1−DMECH)α0where S0 and α0 arematerial parameter. Further simplifying Eq. (58) yields the multiaxial plastic damage model:(59)D˙MECH=ησeq2RvE(1−DMECH)α1p˙where η=12S0, and α1=2α0, can be determined by experiments.

4. Finite-element modeling framework

4.1. FE model design

The microstructure of a polycrystalline material has been incorporated into a finite element (FE) model. To allow the development of intergranular and transgranular cracks in the structure, a two-dimensional model of grain and grain boundary was developed by using Voronoi tessellation and cell offsetting techniques [32]. In the present work, the FE model containing random grains and grain boundary was created with the average grain size of 304 steel given by optical microscope (OM) observation. The generated random grains are shown in Fig. 8, where the average grain size is 58 μm. A finite width of 1 μm is adopted for the pseudo GB as this dimension helps avoid the element distortion [11,12], and corresponding to the size of the corroded GB measured from SEM images. The microstructure with dimension of 0.3 × 0.3 mm^2 is meshed with global size of 2 μm, generating 27593 continuum axis-symmetric quadrilateral elements with reduced integration (CAX4R) in FE models.

The adopted mesh size has been proven to be both accurate and computationally efficient through a mesh sensitivity study. The model was constrained in the x direction (y symmetry boundary condition), and a displacement constraint in the y direction was applied to the top surface of the model.

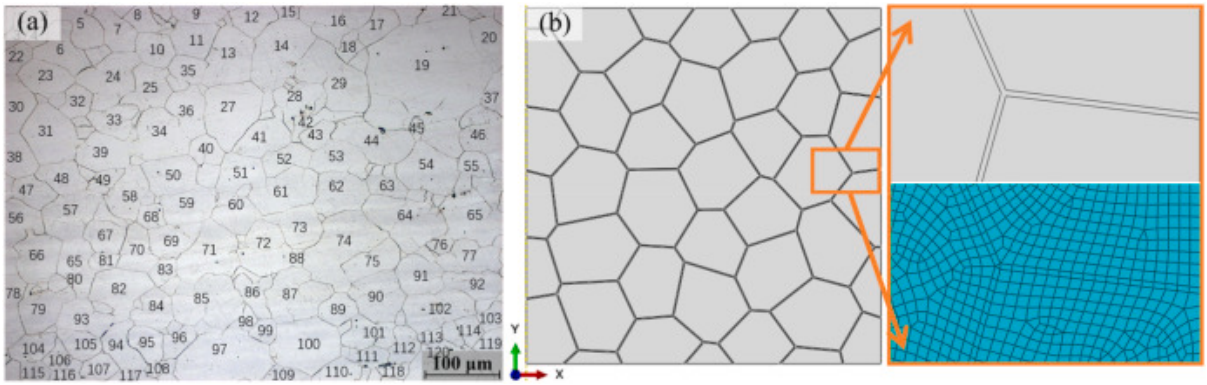

1. Download: Download high-res image (731KB)
2. Download: Download full-size image

Fig. 8. (a) Microstructural of 304 steel and (b) The corresponding FE model.

4.2. Implementation of the model

The increments of stress and effective plastic strain are obtained using the implicit integration scheme. To update all the required quantities regarding the increment in effective plastic strain-rate, Δp, the von Mises equivalent stress, σe, can be given as a function of the equivalent trail stress and Δp [33]:(60)σ˜e=σ˜etr−3GΔpwhere *G* is the shear modulus and, σetr represents the equivalent trial stress. Substituting Eq. (60) into Eq. (3), the accumulated strain-rate can be reformulated according to Eq. (8):(61)p˙=ϕ(Δp,RH)=θsinh[ϕ(σ˜etr−3GΔp−R−σy0)]

Eq. (61) is a typical implicit expression, which can be solved by applying the Newton iterative method. Finally, the iterative increment in effective plastic yields:

where(62)dΔp=ϕ−Δp/Δt1/Δt−ϕΔp−γϕRH(63)∂ϕ∂Δp=ϕΔp=−3Gθϕcoshσetr−3GΔp−RH−σy0)(64)∂ϕ∂RH=ϕR=−θϕcoshσetr−3GΔp−RH−σy0)(65)γ=BQ−RH)

The increment in effective plastic strain is:(66)Δp=Δp+dΔp

The constitutive relationship is implemented within a UMAT user material subroutine. The increment in plastic strain is determined using the flow rule of Eq. (7). Then the increment in stress is calculated as:(67)Δσ=(1−DTOT)Λ:(Δε−Δεe−Δεp)where Λ is the elasticity tensor.

The damage evolution equation is implemented within a USDFLD user subroutine for use with the commercial FE code Abaqus. To evaluate the MSC damage, the distance from the centroids of each FE element to the corroded surface is primarily calculated by pre-processing. Then MSC damage is evaluated for each element during the FE analysis. The expression of plastic damage, i.e. Eq. (59), is a typical implicit equation, which can be solved using the backward Euler method. Once the MSC damage and plastic damage are known, the total damage DTOT for each element is calculated according to Eq. (45). When the value of DTOT is greater than or equal to the random damage threshold DTHrnd, the element is considered to have failed. Using the element deletion technique, the failed element is deleted to simulate cracking. It should be noted that UMAT and USDFLD subroutines are called for at each material integration point at every iteration of each increment. The state variables, such as stress, strain, solution-dependent state variables will be transferred between each other when they are called.

5. Modelling results and discussion

5.1. Verifying the corrosion kinetic model incorporation of impurity

A linear relationship between the concentration of chloride impurity and corrosion rate constants is given in section 3.2.1. Two unknown parameters should be determined the corrosion rate constant $k_{p0,}$ which is independent of chloride impurity, and the material dependent coefficient λ. The corrosion rate constants for different austenitic stainless steels in solar salt containing different contents of chloride impurity (SS, SS_0.6, SS_1.0 and SS_1.4) were provided in previous experimental investigation. The parameters k_{p0} and λ can be determined using two of the corrosion rate constants, and verified with the remaining data. In this case, the corrosion rate constants from the corrosion tests on SS and SS_1.0 were used to determine the parameters. The determined parameters and the predicted k_p-C_{Cl}-curve for 304, 316L and 347 steels are presented in Fig. 9. The measured k_p values [16,34]show good agreement with the predicted results and increase linearly with the concentrations of chloride impurity.

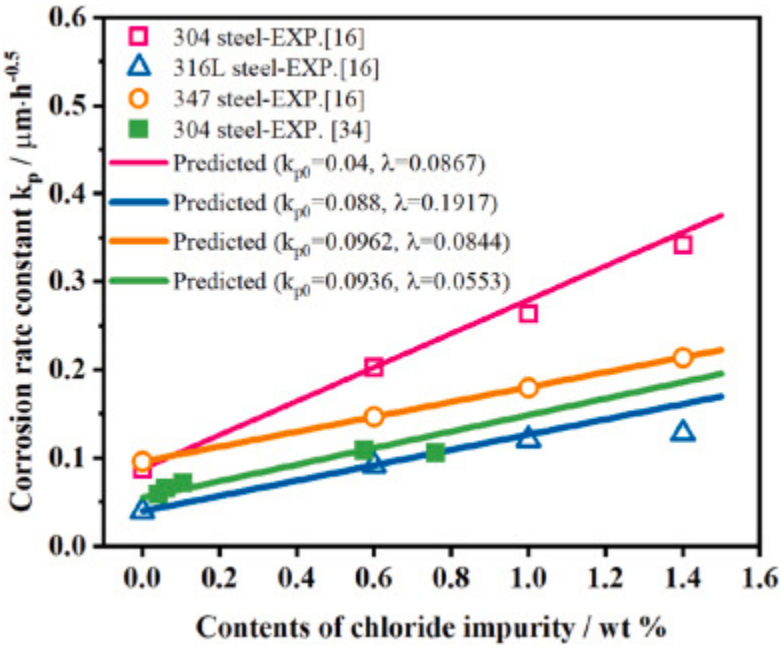

1. Download: Download high-res image (462KB)
2. Download: Download full-size image

Fig. 9. Comparison between the predicted k_p-C_{Cl}-curve and the measured k_p.

5.2. Determination of material parameters

A step-by-step procedure is employed to identify the required material parameters in plastic damage model. The elastic material parameters of Young's modulus, E, Poisson's ratio, v, and initial yield stress, σ_{y0}, can be determined from uniaxial tensile curves. Once the elastic constants have been determined, the isotropic hardening parameters Q can be estimated by the difference between the saturated value of R and σ_{y0}. The isotropic hardening parameter B is then determined using the least squares method. For the viscoplastic material parameters θ and ϕ, which can be obtained from long-term creep data [22]. However, due to the limited availability creep data for the specific materials and temperature in this study, uniaxial tensile tests were performed at three different strain rates at 565 °C. By fitting the hardening parts of these three stress-strain curves, the initial values of θ and ϕ, i.e. θ_0 and ϕ_0 can be determined. Using the Levenberg-Marquardt optimization approach, the material parameters θ, ϕ, η and α_1 are then fitted to the SSRT data obtained in air.

The parameters related to the MSC damage, such as the exponent of damage distribution, β, the width

of MSC affected area, c, and the diffusion coefficient of cations, D_c, will be identified by long-term corrosion tests. Due to the depletion of Cr underneath the corrosion layer, the distribution of Cr from corrosion layer to substrate can be used to determine the exponent of damage distribution, β. First, the normalized concentration of Cr, CcrNor, can be obtained from EPMA line scan of the corrosion-affected area (as shown in Fig. 3). The constant β, can then be determined by fitting the scatter plot of (1-CcrNor, *distance*) using a power law function. The width of MSC affected area, c, which corresponds to the width of the Cr-depletion area, can be estimated from the EPMA line scan results. The diffusion coefficient of cations in the corrosion layer, D_c, is challenging to measure experimentally. According to Eqs. (38), (40), D_c, can be determined when the stress-strain curve and corrosion kinetic data of the grain under SSRT are provided. By inputting the stress and accumulated strain increments, the constant D_c can be obtained by fitting the corrosion kinetic data from the SSRT test (as shown in Fig. 5). In addition, D_{th} can be determined from the tensile curve. As shown in Fig. 10, the damage increases rapidly when the value reaches 0.4. Hence, it is reasonable to assign a value of 0.4 to D_{th} as the threshold. The procedure for parameter identification and determination is shown in Fig. 10. All the determined material parameters are presented in Table 1.

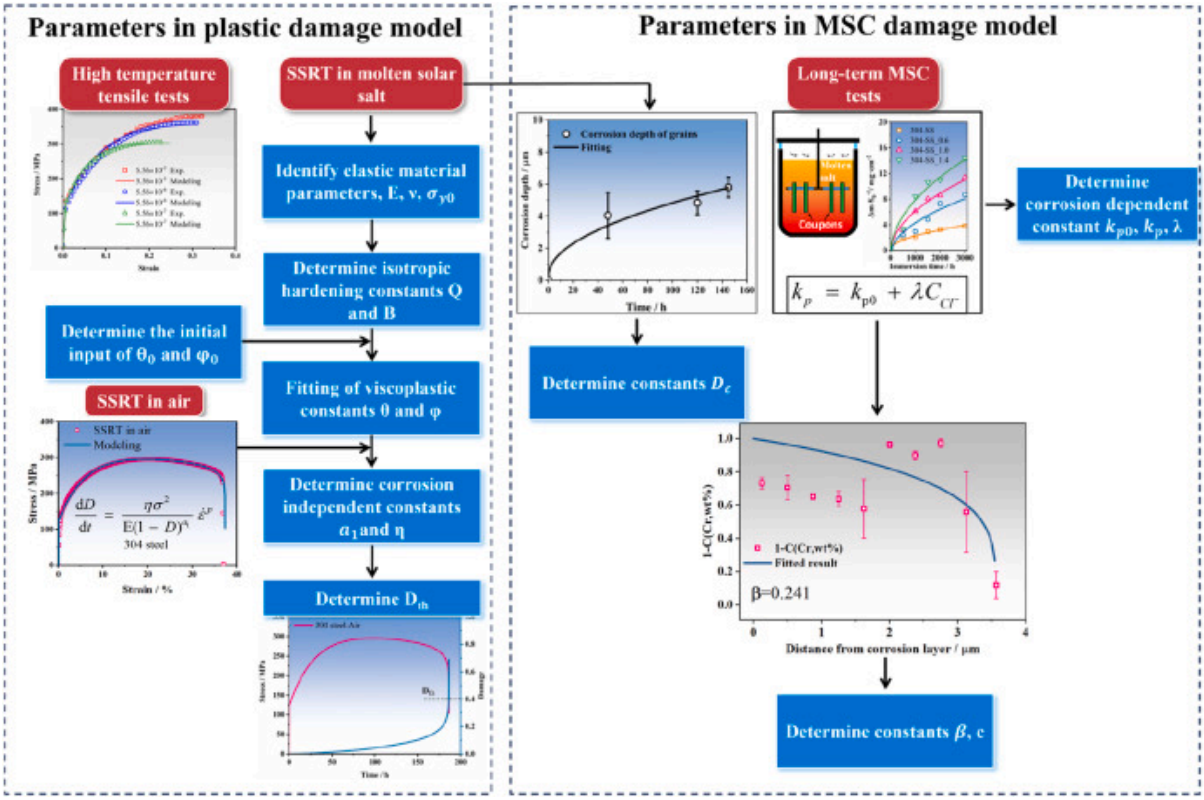

1. Download: Download high-res image (847KB)
2. Download: Download full-size image

Fig. 10. Schematic diagram of the parameter determination process.

Table 1. Material constants in molten salt corrosion-tensile damage constitutive model.

Properties	Symbol	Value
	E	168 GPa
	v	0.3

Properties	Symbol	Value
	θ	1.04×10^{-3} MPa^{-1}
Elastic-plastic	ϕ	8.03×10^{-5} s-1
properties	Q	178.3 MPa
	B	16.8 MPa
	σp	129.4 MPa
Damage properties	η	0.41
	a_1	14.4
	D_{th}	0.4
	β	0.241
	c	4 μm
	D_c	8.07 μm^2 s^{-1}
Constants	T	838 K
	V_m	7.12×10^{-6} m^3 mol^{-1}
	R	8.314 J $(mol \cdot K)^{-1}$
	ε_0	0.002
	Ω_m	1.1×10^{-29}
	Φ	2.13 [35]
	k	1.38×10^{-23} J K^{-1}

5.3. Modeling of molten salt corrosion

The distance from the closet surface (as indicated by the arrow in Fig. 11, surface A) was computed for each element at the beginning of the simulation, as illustrated in Fig. 11(a). The closet surface is in contact with the molten salt. A uniform distribution of random threshold damage in the range of 0.36–0.44 was generated for each element during the analysis, as shown in Fig. 11(b). Due to the differences in damage threshold for each element, random corrosion and cracking of the model can be simulated.

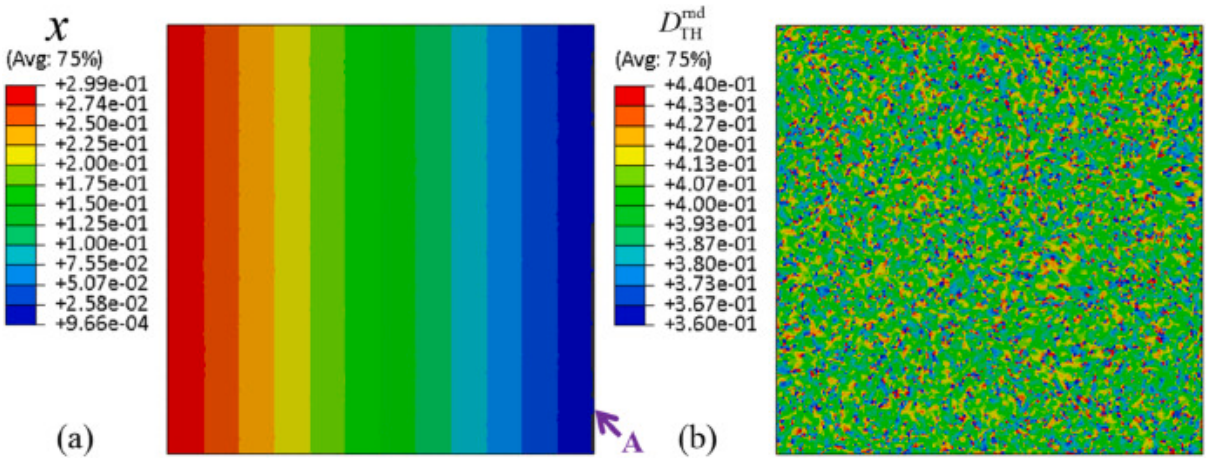

1. Download: Download high-res image (1MB)
2. Download: Download full-size image

Fig. 11. (a) The distance (x) of elements from the closet surface; (b) The contour of random critical damage (DTHrnd) for elements.

Fig. 12(a) shows the corrosion morphology of the tested sample under SSRT in molten salt environment at 48 h. Due to the micro-scale variability, an uneven corrosion layer/substrate interface formed on the surface. Corrosion of grain boundary is evident, leading to oxide intrusions greater than 20 μm in depth. The grain boundary is fully corroded near the surface but only partially corroded farther away, indicating that corrosion depends on the distance from the surface in contact with molten salt. Fig. 12(b) presents the modeling result of total damage distribution, which shows a gradient gradient in the depth direction of grains. The fully damaged area corresponds to the corrosion layer, while the partially damaged area reflects the Cr-depletion zone. The damage depth at the GB is about 25 μm, matching well with the cross-sectional morphology. At 120 h, oxide intrusions extend deeper into the substrate and along branches at GB triple points, as highlighted by the yellow dash line in Fig. 12(c). The predicted damage distribution aligns well with the obseved corrosion morphology at 120 h, as shown in Fig. 12(d).

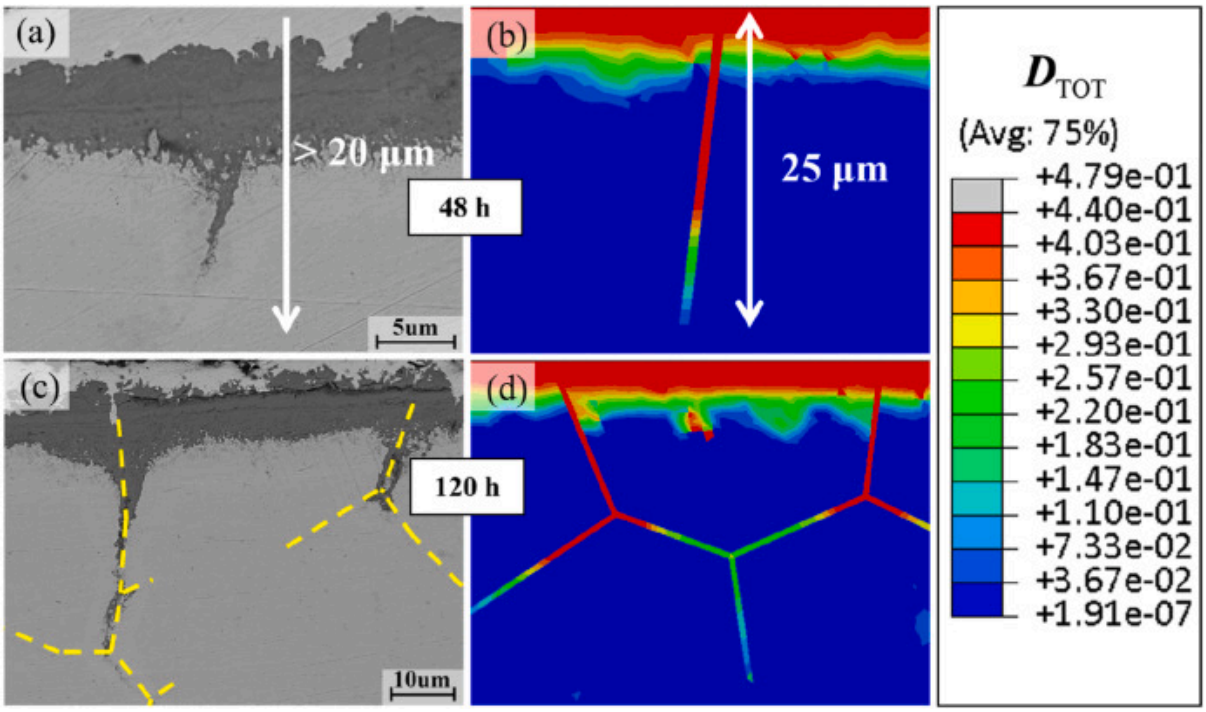

1. Download: Download high-res image (772KB)
2. Download: Download full-size image

Fig. 12. Comparison of the cross-sectional morphologies of tested sample after different times with FE results: (a) and (b) 48 h; (c) and (d) 120 h.

Fig. 13 shows the comparison between the modeled corrosion kinetic curve for a grain and experiment data under SSRT. Each point represents the average value of the corrosion layer thickness obtained from three BSE images at different sites in the tested sample. It is evident that the predicted corrosion kinetic curve follows a parabolic law, which is consistent with experimental results. These findings demonstrate that the proposed corrosion kinetic model for grain and GB accuracyly models the corrosion behavior of stainless steel in molten salt under SSRT conditions.

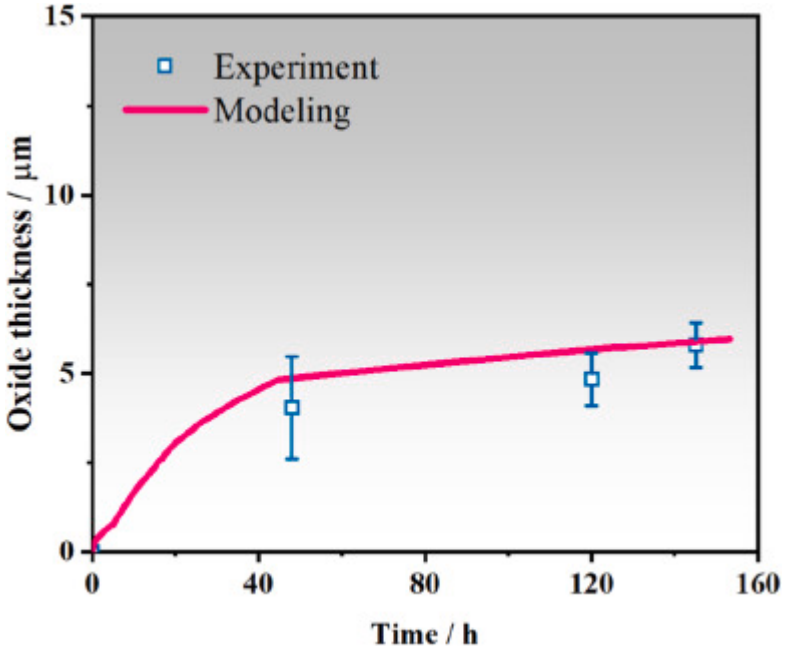

1. Download: Download high-res image (237KB)
2. Download: Download full-size image

Fig. 13. Comparison of the modeling corrosion kinetic curve with experimental results.

5.4. Prediction of molten salt corrosion cracking

Fig. 14(a) shows the corrosion cracking morphology of 304 stainless steel under SSRT in molten salt at 148 h. It is clear that the cracks propagate along the corroded grain boundaries. According to Fig. 6, corrosion of GBs and the growth of oxide occur at the initiate stage during SSRT. However, the brittle oxide in GBs has negligible load-bearing capacity, leading to the cracking of oxide under continuous deformation. As a result, the fresh substrate ahead of the crack tip will be exposed to the molten salt environment, causing further corrosion of GBs. Due to the stress concentration, the corroded GBs are prone to cracking. This cycle of corrosion and cracking of GBs continues untill the sample fails. Fig. 14(b) shows the contour of the von Mises stress distribution under SSRT load, taking molten salt corrosion into account. Surface depletion and multi-sites of intergranular cracking from the surface are well simulated. In addition, stress concentration ahead of the crack tips promotes oxide growth in the GB due to the stress dependence of ions diffusion. Fig. 14(c) shows the distribution of molten salt corrosion damage. The simulation accurately captures the uneven surface corrosion damage. In particular, corrosion damage evolves ahead of the crack tips. Under the combined effect of corrosion damage and plastic damage, cracks initiate and propagate in the corrosion-damaged GBs. The

modeling results validate the corrosion cracking mechanism of stainless steel in molten salt under SSRT. However, it should be noted that the present model is proposed based on the solid diffusion of ions in molten nitrate salt. If this model is to be applied in other molten salt systems, it will require some modifications due to the significantly different corrosion mechanisms compared to those addressed in the present study.

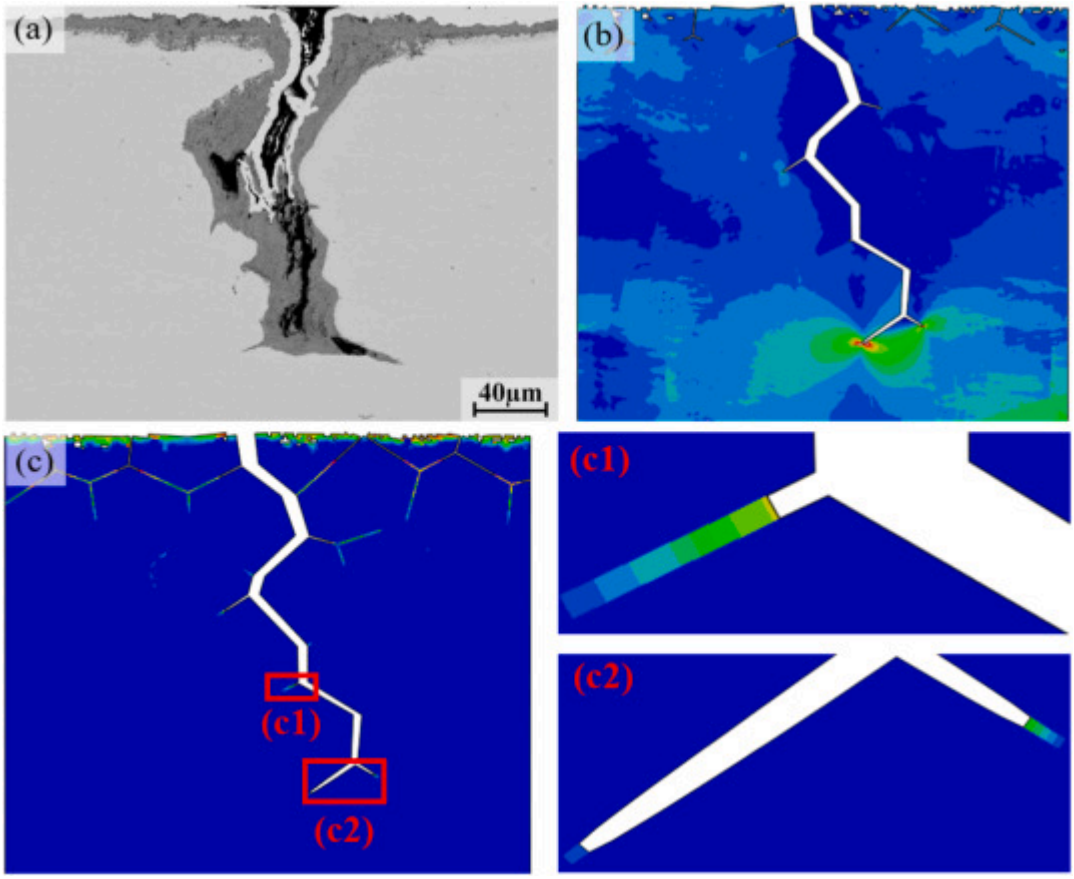

1. Download: Download high-res image (570KB)
2. Download: Download full-size image

Fig. 14. Comparison of experimental results with predicted results after 148 h: (a) The cross-sectional morphology of the sample; (b) Stress distribution; (c) Distribution of molten salt corrosion damage.

6. Conclusions

In this investigation, a corrosion cracking mechanism-based model was proposed for predicting the corrosion and cracking behavior of austenitic stainless steel in molten solar salt under SSRT. First, a corrosion kinetic model was proposed, coupling two corrosion-affected factors: chloride impurity and deformation, which are typical service conditions for austenitic stainless steel in TES systems. Then, the MSC damage of the steel was quantitatively described by the corrosion depth and the distance of materials points from the corrosion surface. Based on the proposed corrosion kinetic model, MSC damage model, plastic damage model, and elastic-viscoplastic model, the corrosion cracking mechanism-based model was developed and implemented using finite element analysis. The proposed models were verified by the experimental results. Specific conclusions are as follows:

- (1)

The proposed corrosion kinetic models for grain and GB successfully capture the effect of chloride impurity and plastic deformation on corrosion rates.

- (2)

The MSC damage distribution under SSRT showed that the corrosion of GB occurred at higher rate compared with grains, which is in accordance with the cross-sectional morphologies of the studied steel.

- (3)

The proposed corrosion cracking mechanism-based model was implemented using finite element analysis method with user subroutines UMAT and USDFLE. Modeling results show that the corrosion of GB occurred first. Subsequently, the corroded GB cracked, inducing the further evolution of MSC damage ahead of the crack tips. These modeling results reflect the corrosion cracking mechanism of the stainless steel in molten solar salt under SSRT.

- (4)

The simulation of intergranular cracking was realized according to the corrosion kinetic of GBs and the corrosion cracking mechanism, instead of setting the damage threshold to a smaller value compared with grains.

CRediT authorship contribution statement

Heng Li: Writing – original draft, Validation, Software, Methodology. **Yan He:** Investigation, Data curation. **Xinyu Yang:** Methodology, Writing – review & editing. **Dewen Zhou:** Methodology. **Xiaowei Wang:** Supervision, Funding acquisition. **Jianqun Tang:** Validation. **Jianming Gong:** Supervision, Funding acquisition.

Declaration of competing interest

The authors declared that they have no known competing financial interests or personal relationships that could have appeared to influence the work reported in this paper.

Acknowledgement

Heng Li, Yan He, Dewen, Zhou, Xiaowei Wang, Jianqun Tang, Jianming Gong gratefully acknowledge the National Natural Science Foundation of China (No.52375149), National Natural Science Foundation of China (No. U21B2077). Xinyu Yang acknowledges the financial support of the Structural Metal Alloys Program (Grant No. A18B1b0061) of Agency for Science, Technology and Research (A*STAR).

Appendix A. Supplementary data

The following is the Supplementary data to this article:Download: Download Word document (687KB)

Multimedia component 1.

References

1. [1]

J.M. Kluger, M.N. Haji, A.H. Slocum

The power balancing benefits of wave energy converters in offshore wind-wave farms with energy storage

Appl. Energy, 331 (2023), Article 120389

View PDFView articleView in ScopusGoogle Scholar

2. [2]

M. Mubarrat, M.M. Mashfy, T. Farhan, M.M. Ehsan

Research advancement and potential prospects of thermal energy storage in concentrated solar power application

International Journal of Thermofluids, 20 (2023), Article 100431

View PDFView articleView in ScopusGoogle Scholar

3. [3]
C.W. Forsberg
Variable and assured peak electricity production from base-load light-water reactors with heat storage and auxiliary combustible fuels
Nucl. Technol., 205 (2018), pp. 377-396
Google Scholar
4. [4]
G. Alva, Y. Lin, G. Fang
An overview of thermal energy storage systems
Energy, 144 (2018), pp. 341-378
View PDFView articleView in ScopusGoogle Scholar
5. [5]
R.E. Grabke H J, M. Spiegel
The effects of chlorides, hydrogen chloride, and sulfur dioxide in the oxidation of steels below deposits
Corrosion Sci., 37 (1995), pp. 1023-1043
Google Scholar
6. [6]
S.H. Goods
The effect of a molten nitrate salt environment on the mechanical properties of INCOLOY alloy 800
J. Mater. Energy Syst. (1983), pp. 28-35
View in ScopusGoogle Scholar
7. [7]
S.H. Goods
Slow Strain Rate Testing of 2.25Cr-1Mo in Molten Nitrate Salt, Sandia National Lab
SNL-CA), Livermore, CA (United States) (1983)
Google Scholar
8. [8]
F. Pineda, A. Mallco, F. De Barbieri, C. Carrasco, M. Henriquez, E. Fuentealba, Á.G. Fernández
Corrosion evaluation by electrochemical real-time tracking of VM12 martensitic steel in a ternary molten salt mixture with lithium nitrates for CSP plants
Sol. Energy Mater. Sol. Cell., 231 (2021), Article 111302
View PDFView articleView in ScopusGoogle Scholar
9. [9]
A. Mallco, F. Pineda, M. Mendoza, M. Henriquez, C. Carrasco, V. Vergara, E. Fuentealba, A.G. Fernand ez
Evaluation of flow accelerated corrosion and mechanical performance of martensitic steel T91 for a ternary mixture of molten salts for CSP plants
Sol. Energy Mater. Sol. Cell., 238 (2022), Article 111632
Google Scholar
10. [10]
H. Li, X. Wang, X. Feng, X. Yang, J. Tang, J. Gong, S.B. Leen
On the corrosion cracking of austenitic stainless steel in molten solar salt: experiments and modeling
Sol. Energy Mater. Sol. Cell., 248 (2022), Article 111983
View PDFView articleView in ScopusGoogle Scholar

11. [11]
F. Biglari, K.M. Nikbin
Environmental creep intergranular damage and multisite crack evolution model for engineering alloys
Comput. Mater. Sci., 84 (2014), pp. 267-277
View PDFView articleView in ScopusGoogle Scholar
12. [12]
F.R. Biglari, K.M. Nikbin
A diffusion driven carburisation combined with a multiaxial continuum creep model to predict random multiple cracking in engineering alloys
Eng. Fract. Mech., 146 (2015), pp. 89-108
View PDFView articleView in ScopusGoogle Scholar
13. [13]
L. Zhao, K.M. Nikbin
Characterizing high temperature crack growth behaviour under mixed environmental, creep and fatigue conditions
Mater. Sci. Eng., A, 728 (2018), pp. 102-114
View PDFView articleView in ScopusGoogle Scholar
14. [14]
C.W.M. Bradshaw R W
Effect of Chloride Content of Molten Nitrate Salt on Corrosion of A516 Carbon Steel
Sandia National Laboratories (SNL), Albuquerque, NM, and Livermore, CA (United States) (2010)
Google Scholar
15. [15]
C. Prieto, J. Gallardo-González, F.J. Ruiz-
Cabañas, C. Barreneche, M. Martínez, M. Segarra, A.I. Fernández
Study of corrosion by Dynamic Gravimetric Analysis (DGA) methodology. Influence of chloride content in solar salt
Sol. Energy Mater. Sol. Cell., 157 (2016), pp. 526-532
View PDFView articleView in ScopusGoogle Scholar
16. [16]
H. Li, X. Yang, X. Yin, X. Wang, J. Tang, J. Gong
Effect of chloride impurity on corrosion kinetics of stainless steels in molten solar salt for CSP application: experiments and modeling
Oxid. Metals, 95 (2021), pp. 311-332
CrossrefView in ScopusGoogle Scholar
17. [17]
H. Li, X. Wang, X. Yin, X. Yang, J. Tang, J. Gong
Corrosion and electrochemical investigations for stainless steels in molten Solar Salt: the influence of chloride impurity
J. Energy Storage, 39 (2021), Article 102675
View PDFView articleView in ScopusGoogle Scholar
18. [18]
H.J. Grabke, S.M. Reese E
The effects of chlorides, hydrogen chloride, and sulfur dioxide in the oxidation of steels below deposits

Corrosion Sci., 37 (1995), pp. 1023-1043
View PDFView articleView in ScopusGoogle Scholar
19. [19]
H. Li, X. Yang, X. Yin, J. Tang, J. Gong, C. Fuyang
Effects of constant load on corrosion cracking of 304 ASS at 600°C in molten salts
Mater. Corros., 71 (2019), pp. 938-948
CrossrefGoogle Scholar
20. [20]
A. Bonk, D. Rückle, S. Kaesche, M. Braun, T. Bauer
Impact of Solar Salt aging on corrosion of martensitic and austenitic steel for concentrating solar power plants
Sol. Energy Mater. Sol. Cell., 203 (2019), Article 110162
View PDFView articleView in ScopusGoogle Scholar
21. [21]
O. Muránsky, I. Karatchevtseva, A.E. Danon, R. Holmes, P. Huai, Z. Zhang
Impact of dislocations and dislocation substructurals on molten salt corrosion of alloys under plasticity-imparting conditions
Corrosion Sci., 176 (2020), Article 108915
View PDFView articleView in ScopusGoogle Scholar
22. [22]
R.A. Barrett, P.E. O'Donoghue, S.B. Leen
An improved unified viscoplastic constitutive model for strain-rate sensitivity in high temperature fatigue
Int. J. Fatig., 48 (2013), pp. 192-204
View PDFView articleView in ScopusGoogle Scholar
23. [23]
A. Soleimani Dorcheh, R.N. Durham, M.C. Galetz
Corrosion behavior of stainless and low-chromium steels and IN625 in molten nitrate salts at 600 °C
Sol. Energy Mater. Sol. Cell., 144 (2016), pp. 109-116
View PDFView articleView in ScopusGoogle Scholar
24. [24]
Y.L. Yao
Thermodynamics of parabolic time rate law of oxidation of metals
J. Chem. Phys., 43 (1965), pp. 3050-3051
CrossrefView in ScopusGoogle Scholar
25. [25]
W. Jost
Diffusion and electrolytic conduction in crystals (ionic semiconductors)
J. Chem. Phys., 1 (1933), pp. 466-475
View in ScopusGoogle Scholar
26. [26]
H. Eyring, S.H. Lin, S.M. Lin
Basic Chemical Kinetics
John Wiley & Sons, NewYork, USA (1980)

Google Scholar
27. [27]
E.M. Gutman
Surface stress problem in heterogeneous mechanochemical reactions
J. Metastable Nanocryst. Mater., 2–6 (1999), pp. 425-436
View in ScopusGoogle Scholar
28. [28]
H.E. Evans, H.Y. Li, P. Bowen
A mechanism for stress-aided grain boundary oxidation ahead of cracks
Scripta Mater., 69 (2013), pp. 179-182
View PDFView articleView in ScopusGoogle Scholar
29. [29]
D. Krajcinovic, J. Lemaitre
Continuum Damage Mechanics Theory and Application
(1987)
Google Scholar
30. [30]
C.J.L. Lemaitre J
Mechanics of Solid Materials
Cambridge University Press (1994)
Google Scholar
31. [31]
D.-g. Shang, W.-x. Yao
Study on nonlinear continuous damage cumulative model for uniaxial fatigue
ACTA AERONAUTICA ET ASTRONAUTICA SINICA-SERIES A AND B-, 19 (1998), pp. 647-656
View in ScopusGoogle Scholar
32. [32]
M. Pettina
Multiscale predictive modelling of ultra-high temperature structural ceramics [D]Mechanical Engineering
Imperial College London (2017)
Google Scholar
33. [33]
F.P.N. Dunne
Introduction to Computational Plasticity
OUP Oxford (2005)
Google Scholar
34. [34]
S.H. Goods, R.W. Bradshaw
Corrosion Resistance of Stainless Steels during Thermal Cycling in Alkali Nitrate Molten Salts
Sandia National Laboratories (SNL), Albuquerque, NM, and Livermore, CA (United States) (2001)
Google Scholar
35. [35]
R.D. Hanbury, G.S. Was

Oxide growth and dissolution on 316L stainless steel during irradiation in high temperature water
Corrosion Sci., 157 (2019), pp. 305-311
View PDFView articleView in ScopusGoogle Scholar